Research Article Vol. 6, No. 9 / September 2019 / Optica 1246

Multifunctional integrated photonics in the mid-infrared with suspended AlGaAs on silicon

Jeff Chiles,[1,*] Nima Nader,[1] Eric J. Stanton,[1] Daniel Herman,[1,2] Galan Moody,[1] Jiangang Zhu,[3] J. Connor Skehan,[1,7] Biswarup Guha,[4,5] Abijith Kowligy,[2,6] Juliet T. Gopinath,[2,3] Kartik Srinivasan,[4] Scott A. Diddams,[2,6] Ian Coddington,[1] Nathan R. Newbury,[1] Jeffrey M. Shainline,[1] Sae Woo Nam,[1] and Richard P. Mirin[1]

[1]NIST, Applied Physics Division, 325 Broadway, Boulder, Colorado 80305, USA
[2]University of Colorado Boulder, Department of Physics, Boulder, Colorado 80309, USA
[3]University of Colorado Boulder, Department of Electrical and Computer Engineering, Boulder, Colorado 80309, USA
[4]NIST, Center for Nanoscale Science and Technology, 100 Bureau Dr, Gaithersburg, Maryland 20899, USA
[5]Maryland Nanocenter, University of Maryland, College Park, Maryland 20742, USA
[6]NIST, Time and Frequency Division, 325 Broadway, Boulder, Colorado 80305, USA
[7]Current address: EPFL, Route Cantonale, 1015 Lausanne, Switzerland
*Corresponding author: jeffrey.chiles@nist.gov

Received 6 May 2019; revised 6 August 2019; accepted 20 August 2019 (Doc. ID 364824); published 18 September 2019

The microscale integration of mid- and long-wave-infrared photonics could enable the development of fieldable, robust chemical sensors, as well as highly efficient infrared frequency converters. However, such technology would be defined by the choice of material platform, which immediately determines the strength and types of optical nonlinearities available, the optical transparency window, modal confinement, and physical robustness. In this work, we demonstrate a new platform, suspended AlGaAs waveguides integrated on silicon, providing excellent performance in all of these metrics. We demonstrate low propagation losses within a span of nearly two octaves (1.26–4.6 μm) with exemplary performance of 0.45 dB/cm at $\lambda = 2.4$ μm. We exploit the high nonlinearity of this platform to demonstrate 1560 nm-pumped second-harmonic generation and octave-spanning supercontinuum reaching out to 2.3 μm with 3.4 pJ pump pulse energy. With mid-IR pumping, we generate supercontinuum spanning from 2.3 to 6.5 μm. Finally, we demonstrate the versatility of the platform with mid-infrared passive devices such as low-loss 10 μm-radius bends, compact power splitters with 96 ± 1% efficiency, and edge couplers with 3.0 ± 0.1 dB loss. This platform has strong potential for multifunctional integrated photonic systems in the mid-infrared. © 2019 Optical Society of America under the terms of the OSA Open Access Publishing Agreement

https://doi.org/10.1364/OPTICA.6.001246

1. INTRODUCTION

The mid- and long-wave-infrared (mid-IR and LWIR) spectral regions from $\lambda = 3$–8 and 8–15 μm are critical spectral regions for sensitive spectroscopic analysis of a variety of physical compounds, such as complex molecular solids, gaseous species, and liquid mixtures [1]. Optical frequency combs in particular have been used to achieve broadband spectroscopy with exquisite frequency resolution [2–8]. However, broadband mid-IR comb technology is still maturing, and nearly all systems would greatly benefit from increased spectral coverage, lower power operation, and improved robustness. Consequently, there has been a consistent push over the past decade to transition mid-IR comb systems or subsystems to compact and robust chip-scale platforms [9–22]. In particular, the small modal area and long propagation lengths of integrated nanophotonic waveguides motivate the development of integrated frequency converters to extend the spectral reach of combs, often with negligible power burdens.

The successful development of integrated mid-IR photonic systems for these applications will ultimately depend on many factors, such as the material platform. Only a small subset of materials has suitable optical transparency [23], and strong optical nonlinearities are also required for the generation or broadening of frequency combs in the mid-IR [15]. While significant Kerr nonlinearity is present in silicon, germanium, and chalcogenide materials, they lack intrinsic second-order optical nonlinearities for highly efficient frequency conversion [6,7,24,25] and electro-optic modulation [26].

Alternatively, group III-V materials possess many desirable properties for multifunctional integrated photonic systems, including a high refractive index, strong second- and third-order optical nonlinearities, and wide optical transparency windows into the LWIR. A practical advantage of these materials is the ability to grow a chemically selective etch stop underneath a high-quality epitaxial device (donor) film, enabling wafer or

chip-bonding film transfer techniques for heterogeneous integration [27,28]. This has enabled high-index-contrast III-V waveguides on other substrates such as oxidized silicon and sapphire [29–33]. However, to take full advantage of the broad transparency window supported by III-V semiconductors in a high-index contrast environment, it is necessary to pursue alternative geometries such as air-clad suspended waveguides. But even this approach requires a degree of caution, as most materials readily form surface oxide layers that also introduce absorption. Undercut etching has been used to suspend GaAs waveguides engineered for mid-IR difference frequency generation [34]. While this represents a promising step in the development of nonlinear mid-IR photonics with III-V materials, many issues remain, such as the propagation loss in the mid-IR region, atmospheric stability, coupling losses, and amenability to wafer-scale production. Without thick cladding layers protecting the surface, suspended III-V waveguides become susceptible to several strong mid-IR and LWIR absorption bands [35] from surface oxidation.

In this work, we present a new approach to air-clad mid-IR waveguides: suspended AlGaAs on silicon, which is shown schematically in Fig. 1. We employ direct-bonded membranes [36,37], which provide superior mechanical stability and design flexibility thanks to the free choice of geometry and absence of stress-inducing perforations. The issue of surface-oxide losses is addressed by passivating the AlGaAs surfaces with ultrathin films of sputtered silicon nitride (SiN), bringing the loss of waveguides from more than 100 dB/cm (without passivation) to <2.5 dB/cm (after passivation) through most of the mid-IR. The fabrication technique described in this work can also be applied to other III-V materials such as GaAs, GaP and GaN. In the case of GaP and GaN, the larger bandgaps could enable even wider transparency windows. However, due to the relative maturity of its device processing and material growth, we chose AlGaAs as the suspended material here.

The objective of this study is to provide a comprehensive demonstration of this platform's suitability for further development. The work is divided as follows. In Section 2.A, we describe the main fabrication approach to realize $Al_{0.32}Ga_{0.68}As$ (bandgap of $\lambda = 681$ nm) photonic waveguides on a conventional silicon 76 mm-diameter wafer (Fig. 1). In Section 2.B, we report the design and characterization of several passive devices, including microring resonators, compact waveguide bends, inverted taper edge couplers, and multimode interferometer (MMI) 1 × 2 splitter junctions. In Section 2.C, we utilize dispersion-engineered waveguides to achieve second-harmonic generation (SHG) and supercontinuum generation from femtosecond laser sources at low pulse energies, and we compare the results for near-IR and mid-IR pumping. We conclude with a discussion of the platform's merits and prospects for future research. Supplement 1 discusses mid-IR losses from surface states and passivation layers, damage threshold measurements and physical robustness, and the measurement setups.

2. RESULTS

A. Fabrication

A schematic representation of the fabrication process is provided in Fig. 1(d). Throughout this project, several fabrication runs were conducted with variations on the main fabrication flow. The illustrated process captures the essential details of the best-performing variation, on which most of the results of this work are focused. The fabrication process consists of (i) cleaning a silicon handle wafer, (ii) etching trench features where waveguides will be situated, (iii) bonding an epitaxial III-V wafer to the handle (a SiN passivation layer has been applied prior to the bond), (iv) chemically removing the III-V wafer substrate (GaAs) and etch-stop layer ($Al_{0.8}Ga_{0.2}As$), (v) electron-beam lithography and plasma etching of the ridge waveguide features

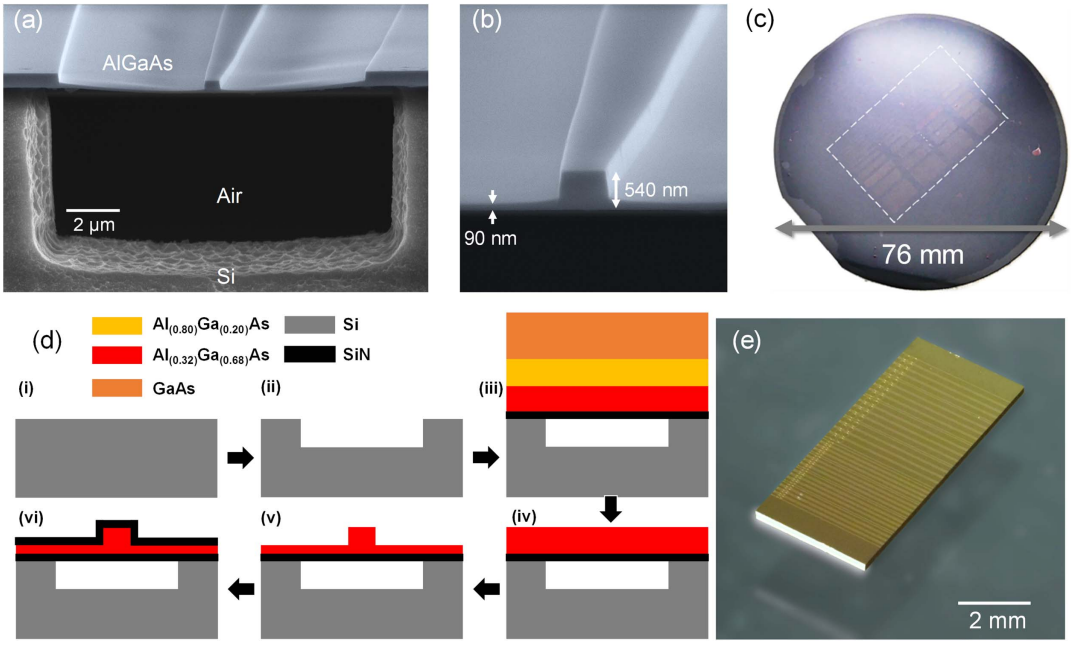

Fig. 1. Suspended AlGaAs on silicon platform. (a), (b) SEM images of a typical waveguide facet produced by dry etching; (c) photograph of a processed wafer prior to die release (an AlGaAs film was bonded over the entire surface, but devices were only fabricated in the middle dashed portion to limit e-beam lithography write time); (d) fabrication flow broken into six essential processing steps; (e) focus-stacked image of a microring resonator die after release from the wafer.

over the trenched areas, and (vi) final oxide strip and top surface passivation with SiN. Afterward, individual dies were released from the wafer simultaneously using deep reactive ion etching (DRIE) through the silicon handle wafer. The dies were then annealed at 300°C in a nitrogen environment, which reduced losses from N-H bond absorption; further discussion is available in Supplement 1. The devices have a nominal core thickness of 540 nm and a slab thickness of 90 nm [Fig. 1(b)]. The trenches underneath the waveguides are 6 μm deep and about 11 μm wide. The SiN barriers on the bottom and top surfaces of the membrane are 10 and 20 nm thick, respectively. No die-level processing was necessary, enabling parallel fabrication of dozens of chips without any polishing and cleaving (which is generally required for sapphire or group III-V substrates). This is a key strength of utilizing silicon substrates.

B. Passive Measurements

High-performance passive devices are required to eventually integrate multiple components on one chip, such as nonlinear frequency converters, modulators, and detectors. The ability to simultaneously realize precisely dispersion-engineered waveguides with tight bending radii, small mode volumes, and low coupling losses is not guaranteed in all waveguide platforms. To this end, we designed, fabricated, and tested several key passive elements, including microring resonators, bends, 1 × 2 MMI power splitters, and input/output (edge) couplers. First, we consider the characterization of suspended AlGaAs microring resonators over a broad wavelength range from the near- to mid-IR. We show that the passivation approach was effective at suppressing the inherently high absorption loss of bare AlGaAs surfaces, achieving losses below 2.5 dB/cm out to $\lambda = 4.6$ μm. An analysis focused on specific loss contributions in the mid-IR, including surface states of unpassivated waveguides, can be found in Supplement 1.

1. Microring Resonators and Propagation Loss

Microring resonators provide a convenient gauge for the waveguiding performance of any integrated photonic platform. Since we are interested in nonlinear applications involving pump wavelengths across the near-IR and mid-IR, we examined the performance of several resonator devices at $\lambda = 1.26$, 1.59, 2.39, 3.64, and 4.56 μm. For all wavelengths, light was aligned to

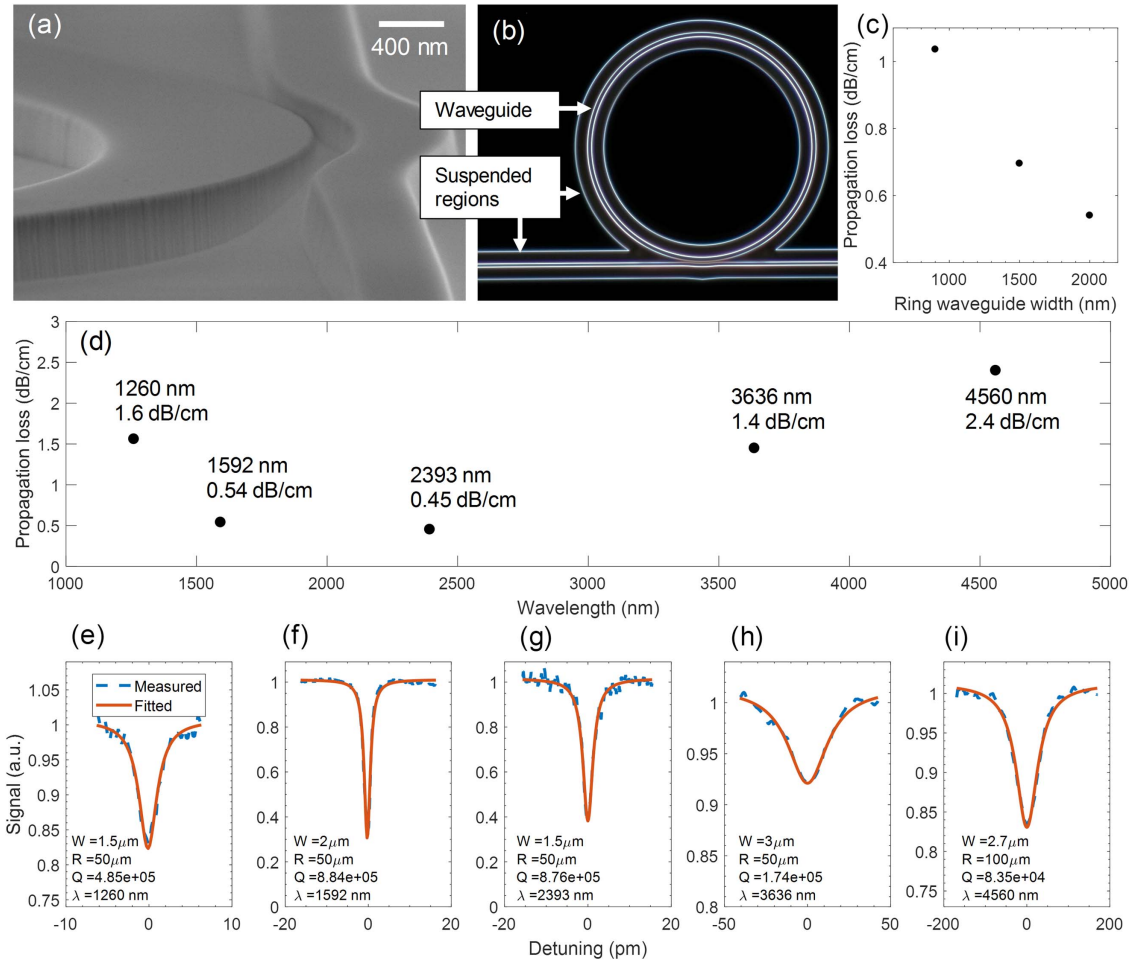

Fig. 2. Characterization of microring resonators. (a) SEM image of a resonator, showing pulley-coupler region and sidewall roughness of a ring; (b) dark-field optical micrograph of the top view of a fabricated resonator. Suspended regions encompass all waveguide features on the substrate. (c) Ring waveguide width versus propagation loss for resonances taken at $\lambda = 1564$, 1556, and 1592 nm, from left to right. (d) Compiled propagation loss data versus wavelength. The first two data points (1260 and 1592 nm) use the intrinsic rather than loaded Q. For the others, the signal was AC-coupled (giving uncertain extinction ratio), so we used loaded Q. (e)–(i) Experimental and fitted traces for the resonance considered in each datapoint of subplot (d). W, width of ring waveguide; R, radius of ring resonator; Q, loaded quality factor.

the quasi-transverse-electric (TE) mode of the waveguides. Further discussion of the measurement setups and laser systems is available in Supplement 1.

The results are collected in Fig. 2. The broadband spectral dependence of propagation loss is shown in Fig. 2(d). The relevant device parameters (ring waveguide width, ring radius, etc.) and measurement results are shown for each resonance in Figs. 2(e)–2(i). The resonances in this figure each represent the highest quality factor (Q) observed for that wavelength point. The maximum loaded Q of 8.8×10^5 is achieved in the 2-μm-wide ring device at $\lambda = 1592$ nm. Factoring out the coupling loss of the ring (conservatively assuming an undercoupled condition), this corresponds to an intrinsic Q of 1.1×10^6, giving a waveguide propagation loss of 0.54 dB/cm. Going to longer wavelengths, we measured propagation losses of 0.45, 1.4, and 2.4 dB/cm for $\lambda = 2.39$, 3.64, and 4.56 μm, respectively. It can be seen that the propagation loss exhibits a trough between $\lambda = 1500$–2500 nm, with a sharply rising loss on the short-wavelength side and a slow increase toward longer wavelengths. The blue-side increase can readily be attributed to the well-known phenomenon of surface-state absorption observed in GaAs/AlGaAs waveguides, which increases sharply at wavelengths near $\lambda = 1$ μm [38]. The fabrication process was not optimized to enhance the performance in this region, but specific treatments are possible if low-loss operation is required here [39]. The loss observed from $\lambda = 1500$–2500 nm is mostly scattering loss. The trend of ring waveguide width versus loss is plotted in Fig. 2(c). It can be seen that the propagation loss does not bottom out even at the widest width considered, showing that sidewall scattering is still a significant contribution to the overall loss. Figure 2(a) shows evidence of sidewall corrugations resulting from roughness in the lithography that is transferred directly to the device, indicated by striations that are uniform along the vertical axis, but varying in position in the width axis of the waveguide. Multipass electron-beam lithography [40] or resist reflow can be employed to mitigate this effect. We discuss long-wavelength losses and possible origins in Supplement 1, including a narrow peak in absorption near $\lambda = 3$ μm that could not be analyzed with ring resonators. As a final note to this section, the ring resonance data were taken more than two months after fabrication of the chips, proving the effectiveness of the passivation layer at preventing losses from oxidation over time.

2. Coupling Loss

In order to achieve efficient frequency conversion with integrated photonic devices, it is critical to have low-loss and broadband on- and off-chip couplers. We pursued inverted taper couplers to meet these goals. The facets are prepared in parallel via plasma etching. An optical micrograph of a typical edge coupler is shown in the lower inset of Fig. 3(a). They employ two stages of tapering [upper inset of Fig. 3(a)], which reduces the total length. We consider several couplers with corresponding wavelengths of interest to this project: 1.55, 2.3, and 4.6 μm. The results are shown in Fig. 3(a), and the coupler geometrical parameters are given in Table 1. In many cases, the taper length did not factor significantly into the performance, but it is included for completeness. The lowest coupling loss of 3.0 ± 0.1 dB is achieved at $\lambda = 4.6$ μm, where this value corrects for the expected propagation loss of 0.2 dB in a 1 mm long chip at this wavelength. The contribution of surface reflection to the loss of this taper tip was estimated to be 1.2%. Experimental losses are reported with respect to the reference transmission of light through both aspheric lenses with no chip. The increase in loss toward shorter wavelengths is expected due to the slab portion constraining the modal extent in the vertical direction. Fully suspended taper geometries may be employed in the future to enhance the performance at shorter wavelengths [37].

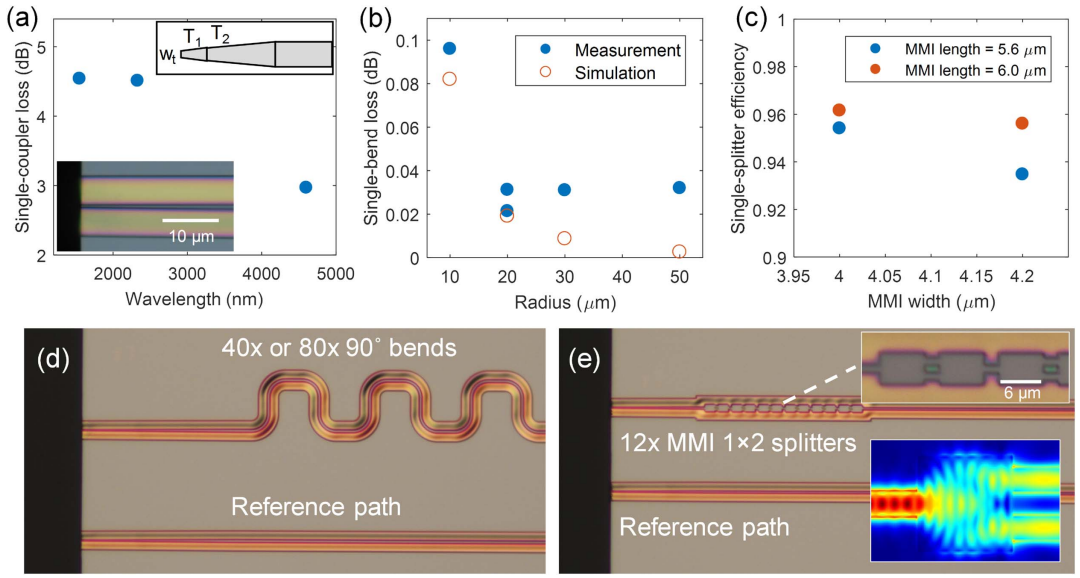

Fig. 3. Experimental characterization of passive suspended AlGaAs components. (a) Loss-per-edge-coupler at different wavelengths. Top inset, inverted taper geometry, showing tip width w_t, and taper sections T_1 and T_2 (see Table 1); bottom inset, optical micrograph of an inverted taper edge coupler; (b) bend radius versus single-bend loss at $\lambda = 4.6$ μm for a 1.4 μm-wide waveguide; (c) experimentally measured MMI power splitter efficiency for several variations on the length and width of the multimode propagation section; (d), (e) optical micrographs of cutback structures used to measure single-bend and single-splitter loss, respectively. Top inset of (e): zoom view of consecutive MMIs. Bottom inset of (e): top view of the simulated optical intensity of the designed MMI splitter.

Table 1. Edge Coupler Geometries

λ (nm)	Tip Width (w_t)	Taper 1 (T_1)	Taper 2 (T_2)
1550	230 nm	to 500 nm over 36 μm	to 1000 nm over 36 μm
2320	210 nm	to 650 nm over 36 μm	to 1000 nm over 31 μm
4600	300 nm	to 550 nm over 15 μm	to 1200 nm over 124 μm

3. Bending Loss

Waveguide bends are an essential element to almost any integrated photonic system, but some material platforms intrinsically limit bending performance based on the lateral or horizontal index contrast, or the typical mode volume required to realize low-loss waveguides. For waveguides that take advantage of strong modal confinement to avoid cladding losses [41], relatively large, graded-curvature bends are required to avoid modal mixing. In other platforms where limited index contrast is available [19], bends are also constrained by leakage losses. With suspended AlGaAs on silicon, however, a strong index contrast can be achieved on all sides of the waveguide, enabling small mode volumes and compact bends. We utilized the structures shown in Fig. 3(d) to test the bending performance. They consist of a reference path with only a straight waveguide, and an adjacent path containing 40 or 80 90° bends, each separated by 10 μm of straight waveguide length, to properly assess the mode transition loss (each bend having two straight-to-bend transitions). Propagation losses are also part of the total loss. These structures were repeated over an array of several widths and radii and tested at both $\lambda = 3.4$ and 4.6 μm. The bend loss dependence on radius at $\lambda = 4.6$ μm is shown in Fig. 3(b), with a typical value of 0.03 dB loss per bend above radii of 20 μm. The waveguide width was 1.4 μm. The experimental values are plotted alongside simulated bend loss values, where one bend in simulations consists of two transitions between straight and bent waveguides. The results are generally in good agreement, and the discrepancy in loss values for larger radii can be explained by additional propagation loss compared to the reference paths. At $\lambda = 3.4$ μm, 0.03 dB loss per bend is experimentally observed for a radius of 20 μm (1.4 μm waveguide width), and 0.06 dB loss per bend at 10 μm radius (1.0 μm waveguide width). For reference, the simulated loss of one 10 μm radius bend at $\lambda = 3.4$ μm (two transitions from straight-to-bent or vice versa) is 0.04 dB, in good agreement, considering the extra loss is likely from sidewall scattering.

4. MMI Splitters

We also investigated 1 × 2 power splitters, another important building block for multifunctional photonic systems in the mid-IR and LWIR regions. We used MMI-type splitters for compactness, as opposed to adiabatic or directional coupler-based designs. The simulated design used the following parameters: MMI length of 6 μm, MMI width of 4 μm, port waveguide width of 1 μm, and output port waveguide center-to-center gap of 2 μm. The simulated efficiency was 90% at $\lambda = 3.4$ μm. The optical intensity from a top view is shown in the lower inset of Fig. 3(e). This device is simulated to maintain better than 90% efficiency (0.46 dB loss) over an optical bandwidth of 3000–3400 nm. This compares well to the (2 × 2) mid-IR power splitters demonstrated in Ref. [14] in terms of insertion loss and bandwidth, but with a footprint about 10 times smaller. We characterized the devices with the structures in Fig. 3(e). They consist of a reference path with only a straight waveguide, and an adjacent path containing 12 consecutive 1 × 2 or 2 × 1 devices. Comparing their transmission at $\lambda = 3.4$ μm, we observed an experimental device efficiency of 96 ± 1%. We also tested several variations in design dimensions, and the overall performance in Fig. 3(c) was robust to variations of several hundred nanometers in the MMI length and width parameters. The difference in performance between the simulated and experimental results could be partly a result of unexpected deviations from the design (such as rounded features from lithography and etching) and partly from error in the reference path normalization.

C. Nonlinear Measurements

Next, we focus on the nonlinear optical characterization. This includes two cases: near-IR-pumped and mid-IR-pumped supercontinuum generation. A detailed discussion of the measurement setups in both cases can be found in Supplement 1, as well as a discussion of the damage thresholds observed during experiments.

1. Near-IR-Pumped Supercontinuum Generation

First, we consider suspended AlGaAs waveguides that are dispersion-engineered to achieve anomalous group velocity dispersion (GVD) near the pump wavelength of 1560 nm [Fig. 4(c)]. The waveguides have a core width of 480 nm (estimated based on scanning electron microscopes SEMs and then increasing the estimated width slightly to obtain anomalous dispersion in simulations), an effective mode area of 0.22 μm^2, and a length of 4 mm. Due to a slight curvature of the etch profile near the waveguide core [Fig. 1(b)], the mode simulations incorporate a sloped region on the sidewalls, as shown in the inset of Fig. 4(c). The pump is an amplified and compressed erbium fiber oscillator with a repetition rate of 160 MHz, a pulse width of 61 fs, and a center wavelength of 1560 nm. Light was coupled in to the chip through an aspheric lens, and out through a single-mode lensed fiber. Figure 4(a) shows the output spectral evolution as the waveguide-coupled pump pulse energy is varied. At 300 fJ pump pulse energy, the waveguide output spectrum exhibited no noticeable broadening compared to the input comb spectrum. The onset of supercontinuum generation was observed near 1.9 pJ, and the spectrum was noticeably saturated by three-photon absorption (3PA) at 15 pJ. We observed octave-spanning supercontinuum generation (at −45 dB level with respect to pump intensity) at a pulse energy of 3.4 pJ (average waveguide-coupled power of 0.5 mW). We also observed a SHG peak near 830 nm for almost all input power levels. This results from phase-mismatched conversion over short lengths on the chip and has been observed in other waveguide platforms possessing nonzero $\chi^{(2)}$ [42,43]. We confirmed this by polarizing the output spectrum in vertical (TM) or horizontal (TE) directions in Fig. 4(b). The peak was TM-polarized. This polarization relationship (TE pump, TM harmonic) is expected for GaAs or AlGaAs waveguides propagating along the $[0\bar{1}\,\bar{1}]$ axis. The low pulse energies required to initiate soliton fission in these waveguides and the simultaneous production of single-spatial-mode supercontinuum and SHG could benefit numerous applications, including frequency combs that could be self-referenced with no amplifiers following the oscillator, or very high repetition-rate systems [44–46]. Significantly stronger SHG can readily be achieved in

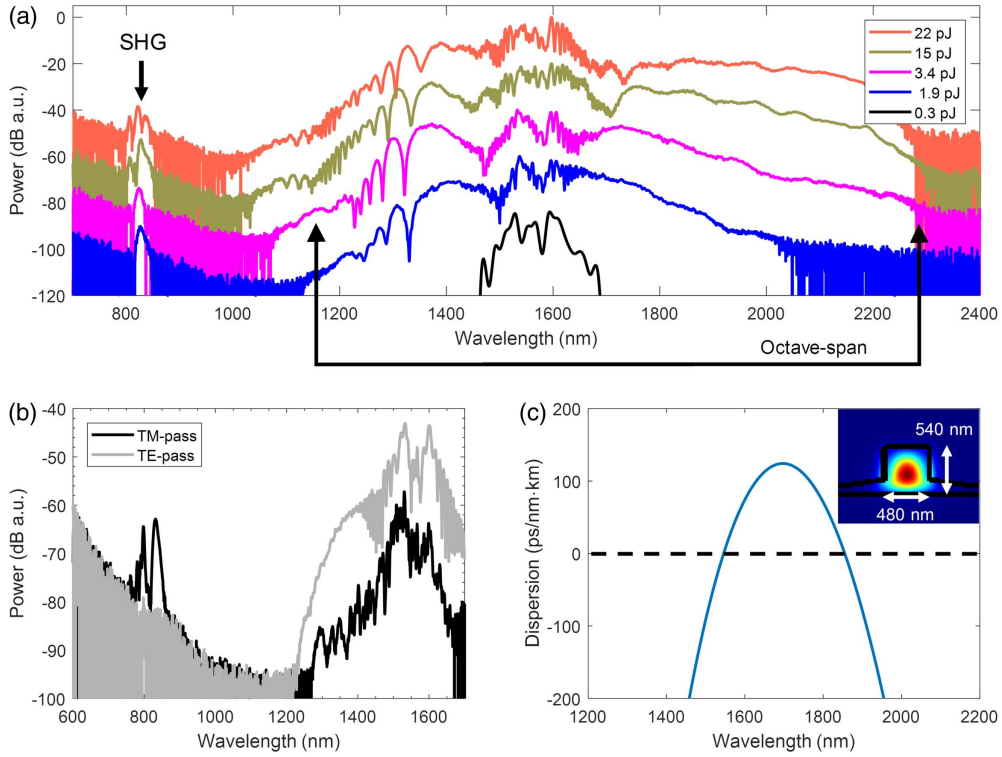

Fig. 4. Supercontinuum generation from a 1560 nm pump. (a) Experimentally measured spectra for different waveguide-coupled pulse energies. Octave-spanning bandwidth is highlighted for the case of 3.4 pJ. Trace-to-trace offset is 20 dB. (b) Polarized supercontinuum output of a similar waveguide for the TE- and TM-pass cases, showing suppression of the second-harmonic peak for TE pass; (c) simulated waveguide GVD; inset, intensity profile for the mode under consideration.

the future through the use of quasi-phase-matching [47,48]. The short-wavelength supercontinuum could also be enhanced via treatments to reduce the short-wavelength losses from surface states on the AlGaAs membrane [39], which we assume to be the current limitation to the bandwidth.

2. Mid-IR-Pumped Supercontinuum Generation

We now consider the broadening of pulsed lasers in the mid-IR region. Here, the pump was produced via difference frequency generation of an amplified and broadened erbium fiber comb output. The nominal pulse width was 85 fs, the repetition rate was 100 MHz, and the center wavelength was 3.06 μm [49]. We focused on a waveguide geometry with a core width of 2.15 μm, an effective mode area of 1.2 μm^2, and a nominal length of 2.3 mm, excluding tapered regions. The GVD and intensity mode profile are depicted in Fig. 5(c), showing a much flatter and broader region of anomalous dispersion compared to the 1550 nm case (owing to the strongly reduced bulk GVD contribution in the mid-IR for AlGaAs). The waveguides were measured by coupling the pump light in the TE-mode orientation and analyzing the output spectrum in a Fourier-transform infrared spectrometer (FTIR). The light was coupled out through an aspheric lens aligned to collimate the long-wave side of the spectrum. More details and a schematic describing the setup can be found in Supplement 1. Figure 5(a) shows the measured spectra at different waveguide-coupled pump pulse energies. At the lowest energy of 11 pJ, the pump exhibited no significant broadening. Supercontinuum generation occurred at 45 pJ, showing a smooth, mostly unstructured spectrum spanning out to 6200 nm with a small dispersive wave peak near 6000 nm. At higher pump powers, the spectrum flattened out and broadened slightly. We also investigated variations on the waveguide length in Fig. 5(b). A fixed waveguide-coupled pulse energy of 67 pJ was used here. As expected, longer waveguides resulted in the generation of more solitons, giving a more structured spectrum as the pulse progressed to a final length of 10.5 mm.

Returning to Fig. 5(a), we compare the experimental versus simulated results for 45 pJ of waveguide-coupled pulse energy. The simulations use an $n^{(2)}$ of 0.9×10^{-17} m^2/W and a uniform propagation loss of 10 dB/cm. Note that this loss is actually confined to a narrow peak near $\lambda = 3$ μm from N-H bond absorption; more details and analysis on it can be found in Supplement 1. The material dispersion was modeled as $n(\lambda, x) = n_{GaAs}(\lambda) - 0.45x$ for $\lambda > 1.1$ μm [50], where n_{GaAs} is the material dispersion of GaAs [51], and x is the mole fraction of aluminum for a given AlGaAs composition. The structure of the simulated spectrum largely agrees with the experiment. The simulation produces a dispersive wave near $\lambda = 6$ μm with a smooth region connecting it to the pump. However, the short-wavelength end of the spectrum has some dissimilar features, such as the absence of a simulated dispersive wave at $\lambda = 2.2$ μm. The location of the dispersive wave is strongly dependent on the zero crossing in the GVD curve, so even a small deviation in the geometry or material dispersion could result in significant changes to the spectrum. This could be resolved with more precise measurements of the AlGaAs core thickness, as well as direct measurements of the refractive index of this particular AlGaAs composition in the mid-IR using spectroscopic ellipsometry.

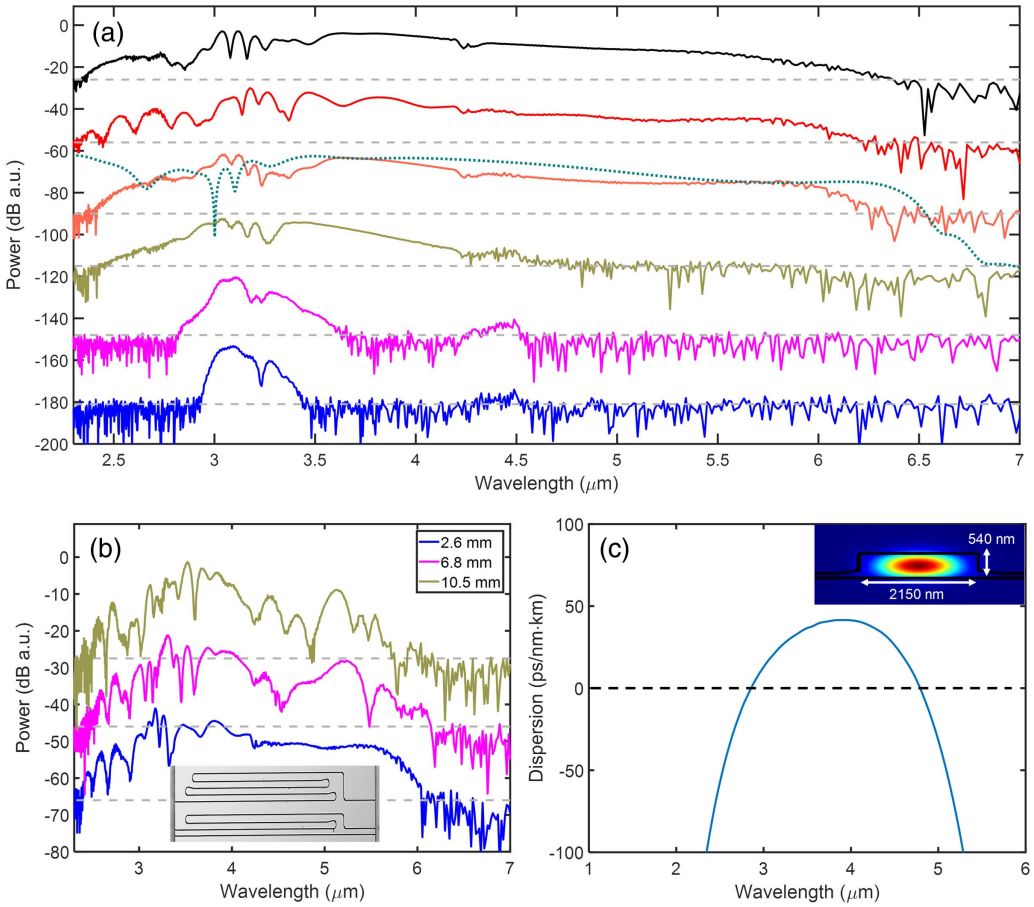

Fig. 5. (a) Supercontinuum generation from a 3060 nm pump; experimentally measured spectra for different waveguide-coupled pulse energies (solid lines), and simulated spectrum at 45 pJ waveguide-coupled pulse energy (dotted line); trace-to-trace offset, 30 dB; (b) supercontinuum output for various total waveguide lengths at 67 pJ pulse energy; trace-to-trace offset, 20 dB; inset, optical micrograph of a paper-clip structure used for length variations. Dashed gray lines in (a, b) indicate approximate noise floor for each trace. (c) Simulated waveguide GVD; inset, intensity profile for the mode under consideration.

In principle, much larger broadening in the long-wave spectrum is expected for waveguides with modified dispersion profiles, such as deeper etches or slightly thicker core regions, which should increase the bandwidth of the anomalous dispersion region. For example, increasing the core thickness of the waveguide by only 20 nm extends the anomalous GVD region to 2.7–5.1 μm instead of 2.9–4.8 μm, producing a redshift by almost 600 nm in the long-wave dispersive wave. The thickness in this work was chosen as a compromise enabling broadband anomalous dispersion to be engineered from $\lambda = 1.5$ to 4.8 μm, depending on the waveguide width. As a final note, in contrast to the 1560 nm pumping case, no SHG was observed for 3060 nm pumping, most likely due to the increased mode area (and thus lower nonlinearity).

3. CONCLUSION

In this work, we presented a new integrated photonic platform: suspended AlGaAs on silicon. By using directly bonded AlGaAs membranes on pre-etched trenches in a silicon substrate, we have overcome many obstacles to the adoption of III-V materials for integrated photonics in the mid-IR. With this approach, multifunctional devices leveraging $\chi^{(2)}$ and $\chi^{(3)}$ nonlinearities can be fabricated reliably at the wafer-scale with high coupling efficiency and low propagation losses. We show the all-around strengths of this platform through a series of linear and nonlinear experiments. The relatively wide bandgap of this AlGaAs composition has enabled us to use near-IR pumps to achieve SHG and octave-spanning supercontinuum generation in dispersion-engineered AlGaAs waveguides at remarkably low waveguide-coupled pulse energies of 3.4 pJ. We also realized octave-spanning supercontinuum generation in the mid-IR, from $\lambda = 2.3$–6.5 μm. High-quality microring resonators were fabricated, and a loss of 0.45 dB/cm was realized at a wavelength of 2.4 μm. A minimum coupling loss of 3.0 ± 0.1 dB/facet was observed at $\lambda = 4.6$ μm. Low-loss passive elements, including compact waveguide bends (0.06 dB loss per 90° bend with 10 μm radius) and 1×2 MMI power splitter junctions with only 6 μm total length and $96 \pm 1\%$ power efficiency have also been demonstrated in the mid-IR. Crucial to the practical development of this platform, we characterized the performance of unpassivated AlGaAs waveguides and showed that proper passivation is essential to low-loss operation in the mid-IR. We developed SiN passivation, allowing waveguides to be operated in air for long time periods (most loss values were measured >2 months after fabrication). All of this has been achieved at the wafer-scale

with no required die-level processing, a valuable practical advantage over native III-V platforms. The combination of a wide optical transparency window, strong $\chi^{(2)}$ and $\chi^{(3)}$ nonlinearities, and the bandgap of 681 nm may enable ultra-efficient frequency converters bridging the gap from the near-IR to the mid-IR. Furthermore, the observed ultralow thresholds for optical nonlinearities, combined with the low propagation losses realized in this work, may point to new opportunities for on-chip quantum photonics [52,53] at 1550 nm and beyond. Suspended AlGaAs on silicon is a high-performance platform for multifunctional integrated photonics with both passive and nonlinear systems.

Funding. Defense Advanced Research Projects Agency (SCOUT, W911NF-15-1-0621); Air Force Office of Scientific Research (FA9550-15-1-0506); National Institute of Standards and Technology.

Acknowledgment. We thank Thorlabs, Inc. for the use of their MLQD4550 QCL product. We also acknowledge FLIR Systems, Inc. for the use of their InSb camera during part of the experiments. We thank the following individuals at NIST Boulder: Esther Baumann, Gabriel Colacion, and Jacob Friedlein for assistance configuring the 1560 nm fiber comb system for nonlinear experiments, Kimberly Briggman for the FTIR measurements, and Paul Blanchard for assistance with SEM imaging. Product disclaimer: Any mention of commercial products is for information only; it does not imply recommendation or endorsement by NIST.

Disclosures. The authors declare that there are no conflicts of interest related to this article.

See Supplement 1 for supporting content.

REFERENCES

1. P. R. Griffiths and J. A. De Haseth, *Fourier Transform Infrared Spectrometry, Vol. 171 of Chemical Analysis: A Series of Monographs on Analytical Chemistry and Its Applications* (Wiley, 2007).
2. F. Adler, M. J. Thorpe, K. C. Cossel, and J. Ye, "Cavity-enhanced direct frequency comb spectroscopy: technology and applications," Ann. Rev. Anal. Chem. **3**, 175–205 (2010).
3. A. Schliesser, N. Picqué, and T. W. Hänsch, "Mid-infrared frequency combs," Nat. Photonics **6**, 440–449 (2012).
4. I. Coddington, N. Newbury, and W. Swann, "Dual-comb spectroscopy," Optica **3**, 414–426 (2016).
5. K. C. Cossel, E. M. Waxman, I. A. Finneran, G. A. Blake, J. Ye, and N. R. Newbury, "Gas-phase broadband spectroscopy using active sources: progress, status, and applications [Invited]," J. Opt. Soc. Am. B **34**, 104–129 (2017).
6. A. V. Muraviev, V. O. Smolski, Z. E. Loparo, and K. L. Vodopyanov, "Massively parallel sensing of trace molecules and their isotopologues with broadband subharmonic mid-infrared frequency combs," Nat. Photonics **12**, 209–214 (2018).
7. H. Timmers, A. Kowligy, A. Lind, F. C. Cruz, N. Nader, M. Silfies, G. Ycas, T. K. Allison, P. G. Schunemann, S. B. Papp, and S. A. Diddams, "Molecular fingerprinting with bright, broadband infrared frequency combs," Optica **5**, 727–732 (2018).
8. N. Picqué and T. W. Hänsch, "Frequency comb spectroscopy," Nat. Photonics **13**, 146–157 (2019).
9. Z. Cheng, X. Chen, C. Y. Wong, K. Xu, and H. K. Tsang, "Mid-infrared suspended membrane waveguide and ring resonator on silicon-on-insulator," IEEE Photon. J. **4**, 1510–1519 (2012).
10. A. Hugi, G. Villares, S. Blaser, H. C. Liu, and J. Faist, "Mid-infrared frequency comb based on a quantum cascade laser," Nature **492**, 229–233 (2012).
11. Y. Yu, X. Gai, T. Wang, P. Ma, R. Wang, Z. Yang, D.-Y. Choi, S. Madden, and B. Luther-Davies, "Mid-infrared supercontinuum generation in chalcogenides," Opt. Mater. Express **3**, 1075–1086 (2013).
12. R. Shankar, I. Bulu, and M. Lončar, "Integrated high-quality factor silicon-on-sapphire ring resonators for the mid-infrared," Appl. Phys. Lett. **102**, 051108 (2013).
13. B. Kuyken, T. Ideguchi, S. Holzner, M. Yan, T. W. Hänsch, J. Van Campenhout, P. Verheyen, S. Coen, F. Leo, R. Baets, G. Roelkens, and N. Picqué, "An octave-spanning mid-infrared frequency comb generated in a silicon nanophotonic wire waveguide," Nat. Commun. **6**, 6310 (2015).
14. J. S. Penades, A. Ortega-Moñux, M. Nedeljkovic, J. G. Wangüemert-Pérez, R. Halir, A. Z. Khokhar, C. Alonso-Ramos, Z. Qu, I. Molina-Fernández, P. Cheben, and G. Z. Mashanovich, "Suspended silicon mid-infrared waveguide devices with subwavelength grating metamaterial cladding," Opt. Express **24**, 22908–22916 (2016).
15. A. G. Griffith, M. Yu, Y. Okawachi, J. Cardenas, A. Mohanty, A. L. Gaeta, and M. Lipson, "Coherent mid-infrared frequency combs in silicon-microresonators in the presence of Raman effects," Opt. Express **24**, 13044–13050 (2016).
16. A. Vasiliev, A. Malik, M. Muneeb, B. Kuyken, R. Baets, and G. Roelkens, "On-chip mid-infrared photothermal spectroscopy using suspended silicon-on-insulator microring resonators," ACS Sens. **1**, 1301–1307 (2016).
17. D. A. Kozak, T. H. Stievater, R. Mahon, and W. S. Rabinovich, "Germanium-on-silicon waveguides at wavelengths from 6.85 to 11.25 microns," IEEE J. Sel. Top. Quantum Electron. **24**, 1–4 (2018).
18. N. Nader, D. L. Maser, F. C. Cruz, A. Kowligy, H. Timmers, J. Chiles, C. Fredrick, D. A. Westly, S. W. Nam, R. P. Mirin, J. M. Shainline, and S. Diddams, "Versatile silicon-waveguide supercontinuum for coherent mid-infrared spectroscopy," APL Photon. **3**, 36102 (2018).
19. J. M. Ramirez, Q. Liu, V. Vakarin, J. Frigerio, A. Ballabio, X. Le Roux, D. Bouville, L. Vivien, G. Isella, and D. Marris-Morini, "Graded SiGe waveguides with broadband low-loss propagation in the mid infrared," Opt. Express **26**, 870–877 (2018).
20. E. J. Stanton, A. Spott, J. Peters, M. L. Davenport, A. Malik, N. Volet, J. Liu, C. D. Merritt, I. Vurgaftman, C. S. Kim, J. R. Meyer, and J. E. Bowers, "Multi-spectral quantum cascade lasers on silicon with integrated multiplexers," in *Conference on Lasers and Electro-Optics (CLEO)* (2019).
21. D. Grassani, E. Tagkoudi, H. Guo, C. Herkommer, F. Yang, T. J. Kippenberg, and C.-S. Brès, "Mid infrared gas spectroscopy using efficient fiber laser driven photonic chip-based supercontinuum," Nat. Commun. **10**, 1553 (2019).
22. L. A. Sterczewski, J. Westberg, M. Bagheri, C. Frez, I. Vurgaftman, C. L. Canedy, W. W. Bewley, C. D. Merritt, C. S. Kim, M. Kim, J. R. Meyer, and G. Wysocki, "Mid-infrared dual-comb spectroscopy with interband cascade lasers," Opt. Lett. **44**, 2113–2116 (2019).
23. R. Soref, "Mid-infrared photonics in silicon and germanium," Nat. Photonics **4**, 495–497 (2010).
24. L. A. Eyres, P. J. Tourreau, T. J. Pinguet, C. B. Ebert, J. S. Harris, M. M. Fejer, L. Becouarn, B. Gerard, and E. Lallier, "All-epitaxial fabrication of thick, orientation-patterned GaAs films for nonlinear optical frequency conversion," Appl. Phys. Lett. **79**, 904 (2001).
25. A. S. Kowligy, A. Lind, D. D. Hickstein, D. R. Carlson, H. Timmers, N. Nader, F. C. Cruz, G. Ycas, S. B. Papp, and S. A. Diddams, "Mid-infrared frequency comb generation via cascaded quadratic nonlinearities in quasi-phase-matched waveguides," Opt. Lett. **43**, 1678–1681 (2018).
26. J. Chiles and S. Fathpour, "Mid-infrared integrated waveguide modulators based on silicon-on-lithium-niobate photonics," Optica **1**, 350–355 (2014).
27. E. Yablonovitch, D. M. Hwang, T. J. Gmitter, L. T. Florez, and J. P. Harbison, "Van der Waals bonding of GaAs epitaxial liftoff films onto arbitrary substrates," Appl. Phys. Lett. **56**, 2419–2421 (1990).
28. H. Park, A. W. Fang, S. Kodama, and J. E. Bowers, "Hybrid silicon evanescent laser fabricated with a silicon waveguide and III-V offset quantum wells," Opt. Express **13**, 9460–9464 (2005).
29. U. D. Dave, C. Ciret, S.-P. Gorza, S. Combrie, A. De Rossi, F. Raineri, G. Roelkens, and B. Kuyken, "Dispersive-wave-based octave-spanning supercontinuum generation in InGaP membrane waveguides on a silicon substrate," Opt. Lett. **40**, 3584–3587 (2015).

30. H. Hu, F. Da Ros, M. Pu, F. Ye, K. Ingerslev, E. Porto da Silva, M. Nooruzzaman, Y. Amma, Y. Sasaki, T. Mizuno, Y. Miyamoto, L. Ottaviano, E. Semenova, P. Guan, D. Zibar, M. Galili, K. Yvind, T. Morioka, and L. K. Oxenløwe, "Single-source chip-based frequency comb enabling extreme parallel data transmission," Nat. Photonics **12**, 469–473 (2018).
31. K. Schneider, P. Welter, Y. Baumgartner, H. Hahn, L. Czornomaz, and P. Seidler, "Gallium phosphide-on-silicon dioxide photonic devices," J. Lightwave Technol. **36**, 2994–3002 (2018).
32. L. Chang, A. Boes, X. Guo, D. T. Spencer, M. J. Kennedy, J. D. Peters, N. Volet, J. Chiles, A. Kowligy, N. Nader, D. D. Hickstein, E. J. Stanton, S. A. Diddams, S. B. Papp, and J. E. Bowers, "Nonlinear optics: heterogeneously integrated GaAs waveguides on insulator for efficient frequency conversion," Laser Photon. Rev. **12**, 1870044 (2018).
33. Y. Zheng, M. Pu, H. K. Sahoo, E. Semenova, and K. Yvind, "High-quality-factor AlGaAs-on-sapphire microring resonators," J. Lightwave Technol. **37**, 868–874 (2019).
34. T. H. Stievater, R. Mahon, D. Park, W. S. Rabinovich, M. W. Pruessner, J. B. Khurgin, and C. J. K. Richardson, "Mid-infrared difference-frequency generation in suspended GaAs waveguides," Opt. Lett. **39**, 945–948 (2014).
35. D. W. Sheibley and M. H. Fowler, "Infrared spectra of various metal oxides in the region of 2 to 26 microns," 1966, https://ntrs.nasa.gov/archive/nasa/casi.ntrs.nasa.gov/19670003469.pdf.
36. J. Chiles, S. Khan, J. Ma, and S. Fathpour, "High-contrast, all-silicon waveguiding platform for ultra-broadband mid-infrared photonics," Appl. Phys. Lett. **103**, 151106 (2013).
37. N. Nader, J. Chiles, H. Timmers, E. J. Stanton, A. Kowligy, A. Lind, S. W. Nam, S. A. Diddams, and R. P. Mirin, "Coherent on-chip frequency combs spanning 1.5–7.5 μm for dual-comb spectroscopy," in *Advanced Photonics (BGPP, IPR, NP, NOMA, Sensors, Networks, SPPCom, SOF)*, OSA Technical Digest (online) (Optical Society of America, 2018), paper NpM4I.8.
38. M. Kaminska, "EL2 defect in GaAs," Phys. Scripta **T19B**, 551–557 (1987).
39. Y. Chang, S. I. Yi, S. Shi, E. Hu, W. H. Weinberg, and J. Merz, "Long-term and thermal stability of hydrogen ion-passivated AlGaAs/GaAs near-surface quantum wells," J. Vac. Sci. Technol. B **13**, 1801–1804 (1995).
40. X. Ji, F. A. S. Barbosa, S. P. Roberts, A. Dutt, J. Cardenas, Y. Okawachi, A. Bryant, A. L. Gaeta, and M. Lipson, "Ultra-low-loss on-chip resonators with sub-milliwatt parametric oscillation threshold," Optica **4**, 619–624 (2017).
41. S. A. Miller, M. Yu, X. Ji, A. G. Griffith, J. Cardenas, A. L. Gaeta, and M. Lipson, "Low-loss silicon platform for broadband mid-infrared photonics," Optica **4**, 707–712 (2017).
42. D. D. Hickstein, H. Jung, D. R. Carlson, A. Lind, I. Coddington, K. Srinivasan, G. G. Ycas, D. C. Cole, A. Kowligy, C. Fredrick, S. Droste, E. S. Lamb, N. R. Newbury, H. X. Tang, S. A. Diddams, and S. B. Papp, "Ultrabroadband supercontinuum generation and frequency-comb stabilization using on-chip waveguides with both cubic and quadratic nonlinearities," Phys. Rev. Appl. **8**, 14025 (2017).
43. M. Yu, B. Desiatov, Y. Okawachi, A. L. Gaeta, and M. Lončar, "Coherent two-octave-spanning supercontinuum generation in lithium-niobate waveguides," Opt. Lett. **44**, 1222–1225 (2019).
44. A. Klenner, A. S. Mayer, A. R. Johnson, K. Luke, M. R. E. Lamont, Y. Okawachi, M. Lipson, A. L. Gaeta, and U. Keller, "Gigahertz frequency comb offset stabilization based on supercontinuum generation in silicon nitride waveguides," Opt. Express **24**, 11043–11053 (2016).
45. T. D. Shoji, W. Xie, K. L. Silverman, A. Feldman, T. Harvey, R. P. Mirin, and T. R. Schibli, "Ultra-low-noise monolithic mode-locked solid-state laser," Optica **3**, 995–998 (2016).
46. D. R. Carlson, D. D. Hickstein, W. Zhang, A. J. Metcalf, F. Quinlan, S. A. Diddams, and S. B. Papp, "Ultrafast electro-optic light with subcycle control," Science **361**, 1358–1363 (2018).
47. A. Rao, J. Chiles, S. Khan, S. Toroghi, M. Malinowski, G. F. Camacho-González, and S. Fathpour, "Second-harmonic generation in single-mode integrated waveguides based on mode-shape modulation," Appl. Phys. Lett. **110**, 111109 (2017).
48. S. Roux, L. Cerutti, E. Tournie, B. Gérard, G. Patriarche, A. Grisard, and E. Lallier, "Low-loss orientation-patterned GaSb waveguides for mid-infrared parametric conversion," Opt. Mater. Express **7**, 3011–3016 (2017).
49. F. C. Cruz, D. L. Maser, T. Johnson, G. Ycas, A. Klose, F. R. Giorgetta, I. Coddington, and S. A. Diddams, "Mid-infrared optical frequency combs based on difference frequency generation for molecular spectroscopy," Opt. Express **23**, 26814–26824 (2015).
50. T. Tamir, G. Griffel, and H. L. Bertoni, *Guided-Wave Optoelectronics: Device Characterization, Analysis, and Design* (Springer, 2013).
51. T. Skauli, P. S. Kuo, K. L. Vodopyanov, T. J. Pinguet, O. Levi, L. A. Eyres, J. S. Harris, M. M. Fejer, B. Gerard, L. Becouarn, and E. Lallier, "Improved dispersion relations for GaAs and applications to nonlinear optics," J. Appl. Phys. **94**, 6447–6455 (2003).
52. A. Cabello and F. Sciarrino, "Loophole-free Bell test based on local precertification of photon's presence," Phys. Rev. X **2**, 21010 (2012).
53. D. R. Hamel, L. K. Shalm, H. Hübel, A. J. Miller, F. Marsili, V. B. Verma, R. P. Mirin, S. W. Nam, K. J. Resch, and T. Jennewein, "Direct generation of three-photon polarization entanglement," Nat. Photonics **8**, 801–807 (2014).

132.163.181.155 {ts '2019-11-07 13:11:06'}